PHYSICAL REVIEW B **102**, 245139 (2020)

Character of the outgoing wave in soft x-ray photoemission

E. E. Krasovskii
Donostia International Physics Center (DIPC), 20018 Donostia/San Sebastián, Basque Country, Spain;
Departamento de Polímeros y Materiales Avanzados: Física, Química y Tecnología, Universidad del Pais Vasco/Euskal Herriko Unibertsitatea, 20080 Donostia/San Sebastián, Basque Country, Spain;
and IKERBASQUE, Basque Foundation for Science, 48013 Bilbao, Basque Country, Spain

(Received 23 September 2020; revised 17 November 2020; accepted 11 December 2020; published 23 December 2020)

Bloch-waves scattering theory is applied to photoemission from Mg(0001) up to photon energies of 320 eV. The quality of various approximations to the photoemission final state is analyzed based on the Fourier decomposition of the *ab initio* time-reversed scattering states. The relative importance of bulk and surface photoeffect in a one-dimensional pseudopotential model and in a real crystal is studied. The crucial role of the lateral umklapp scattering at high energies is revealed, and its implications for the stationary as well as for the attosecond time-resolved photoemission are discussed. The fine structure of the photoemission intensity distribution at high energies observed in earlier experiments is reproduced and explained.

DOI: 10.1103/PhysRevB.102.245139

I. INTRODUCTION

Recent progress in soft x-ray angle-resolved photoemission [1–4] has stimulated interest in the structure of photoelectron final states at kinetic energies of several hundred eV. An important experimental advantage of high energies is the increased photoelectron mean free path [3,5], which has the consequence that the reciprocal-space structure of the outgoing wave normal to the surface becomes better pronounced. Furthermore, with increasing energy the kinetic energy starts dominating the Hamiltonian, and it is believed that at sufficiently high energies the photoelectron motion can be considered free-electron like [1,2,5–10]. At the same time, illuminating evidence of non-free-electron-like behavior of soft x-ray photoelectrons from Al(100) was presented by Strocov [11]. Modern multiple-scattering theory is capable of describing the outgoing photoelectron wave without resorting to any simplifying assumptions about the high-energy wave function. A comprehensive account of the state of the art in the relativistic multiple-scattering theory of photoemission from solids is given in the review articles [12,13] including the discussion of pump-probe excitations and effects of temperature and disorder. The general conclusion is that whereas in the low-energy regime below about 200 eV the electron dynamics is dominated by strong multiple scattering, "with increasing photon energy the final states tend to be more and more free-electron like" [13]. However, clarity is still lacking as to at which energies the transition to the free-electron regime occurs for a given material and how to quantify the closeness of the photoelectron final state to the plane wave.

A precise understanding of this issue is especially important in the emerging field of attosecond spectroscopy [14], where the subfemtosecond duration of the pump pulse implies extreme ultraviolet frequencies. Owing to the overwhelming complexity of the transient photoemission, common theoretical approaches either neglect the interaction of the photoelectron with atomic cores or treat it with a weak one-dimensional (1D) pseudopotential [15–17]. Although limitations of this approximation for energies below 100 eV are well understood, the question of how the structure of the outgoing wave varies on a wide energy scale has not been properly considered so far.

The present paper is an attempt to observe the evolution of the photoelectron wave function in a real system over a wide energy range of 320 eV and see whether it approaches a plane wave. (In terms of angular momentum, this implies the significance of orbitals up to, at least, $l = 10$ in the wave-function expansion in a sphere of 2-a.u. radius.) Magnesium is chosen for this case study as an important object of the attosecond streaking experiments [16–19] (owing to the efficient screening of the laser field in Mg). In addition, the recently measured high-resolution stationary photoemission from Mg(0001) up to $\hbar\omega = 500$ eV [19] presents a perfect example to analyze from the point of view of plane-wave likeness and provides an important verification of the theoretical conclusions.

The best way to assess the validity of an approximation is to compare it with an exact calculation. The present analysis is based on the *ab initio* one-step theory of photoemission [20] implemented via augmented plane waves [21,22]. This computational method employs a straightforward basis-set expansion of the scattering wave function, so the computational cost scales rather unfavorably with energy, which has limited this paper to $\hbar\omega = 320$ eV. However, it provides the unique opportunity to consider the entire interval within the same approach and to clearly see the trends. Owing to a relatively weak atomic potential of Mg, the transfer to a quasifree motion is expected to occur at lower energies than for heavier atoms, so the considered energy interval is representative of a much wider range in other materials. Furthermore, Mg(0001) is an excellent case to assess the performance of the 1D

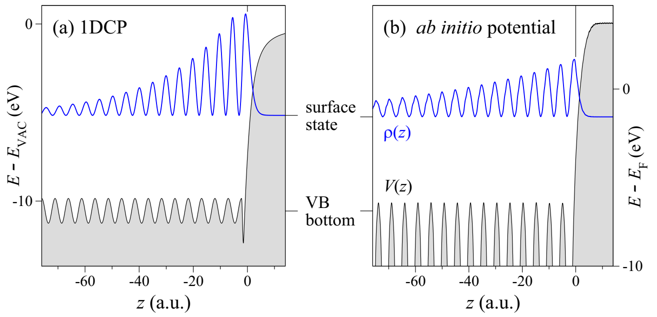

FIG. 1. Crystal potential profile $V(z)$ of the Mg(0001) surface (black lines with shading): (a) 1DCP [23] and (b) *ab initio* potential. Energies of the valence-band (VB) minimum and of the surface state are shown by the ticks on the alternative axes. The blue lines are the density profile $\rho(z)$ of the surface state. The ticks on the top edge indicate the onset of the optical potential $z = 0$.

models: We will take advantage of the 1D Chulkov pseudopotential (1DCP) [23], Fig. 1(a), which perfectly reproduces the occupied $A\Gamma A$ bands of Mg. Here, the one-step theory is comparatively applied to a real crystal with a density-functional-derived potential and to the 1DCP with the aim to understand the role of atomic core scattering. The observed behavior is traced to the Fourier expansion of the all-electron wave functions of the scattering states and is discussed in terms of the quality of the relevant observables.

The present results confirm that the assumption of a free-electron motion at high energies is a reasonable starting point, in the sense that a leading plane wave can be identified in the Fourier expansion of the final state. At the same time, the lattice scattering will be shown to be not negligible over the whole energy range. It manifests itself in a deviation of the **k** vector of the leading wave from the strictly free-electron (SFE) dispersion and in the strong lateral-scattering effect on the outgoing wave: $\Phi^*_{\rm LEED}(\mathbf{r}_\parallel) \neq$ const where LEED stands for low-energy electron diffraction. The latter significantly modifies the fine structure of the photoelectron spectra, and—what is most important for the photoemission timing—it dramatically affects the phases of the transition matrix elements.

The paper is organized as follows: Sec. II gives a brief account of the computational methodology and setup. In Sec. III, the high-energy band structure is discussed. A one-step-theoretical analysis of resonant and nonresonant dipole excitations are presented in Sec. IV. The plane-wave likeness of the scattering states in Mg is discussed in Sec. V. The implication of the wave function composition for the photoelectron escape time are considered in Sec. VI followed by a brief discussion in Sec. VII.

II. THEORY AND COMPUTATIONAL SETUP

Following the one-step theory [20], photoemission is considered as a transition from the initial state ψ to a time-reversed LEED state $\Phi^*_{\rm LEED}$. In the dipole approximation the photocurrent is

$$I(E, \hbar\omega) = \sqrt{E + \hbar\omega - E_{\rm VAC}}\,|\langle\Phi^*_{\rm LEED}|\mathbf{e}\cdot\mathbf{p}|\psi\rangle|^2, \qquad (1)$$

where E is the initial-state energy and $\mathbf{p}$ is the momentum operator. We will consider only the special case when the electric-field vector $\mathbf{e}$ is along the surface normal, so the transition operator reduces to $-i\hbar d/dz$, and the matrix element is the scalar product of $\Phi^*_{\rm LEED}(\mathbf{r})$ and $\psi'_z(\mathbf{r})$. The LEED wave-function $\Phi_{\rm LEED}$ is a scattering solution for a plane wave incident from $+\infty$, and in the crystal half-space where the potential can be considered periodic, it is a superposition of Bloch eigenfunctions $\phi(k, \mathbf{r})$ with (generally) complex surface normal projections k of the Bloch vectors. The latter are referred to as the complex band structure (CBS) of the semi-infinite bulk crystal, which here is obtained with the inverse linear augmented plane-waves (LAPW)-$\mathbf{k}\cdot\mathbf{p}$ method [24]. The inelastic scattering of the outgoing electron is described by the imaginary potential $-iV_{\rm i}$ added to the Hamiltonian in the crystal half-space $z < 0$, see Fig. 1. At sufficiently high energies the surface potential can be approximated by a steplike potential barrier, i.e., the periodic bulk potential is assumed to hold right to the vacuum onset. Then the calculation of $\Phi_{\rm LEED}$ consists in matching its bulk $\phi(k, \mathbf{r})$ expansion to a plane-wave expansion in the vacuum half-space [21]. At lower energies this approximation becomes too rough, and the actual shape of the potential at the surface should be taken into account. In this case scattering wave function is obtained with the variational embedding technique [22], in which the surface barrier is constructed as the potential at the surface of a repeated slab. Thereby, a realistic all-electron potential is employed both in the bulk and at the surface. Exactly the same method is applied to the 1DCP model (only pure plane waves are used as basis functions instead of APWs).

In the LAPW method the space is divided into muffin-tin (MT) spheres and interstitial, and the higher the energy, the higher angular momenta l in the spheres must be considered. By reducing the MT radii the l series can be cut off at a lower $l_{\rm max}$ at the expense of increasing the number of APWs. For the all-electron potential of Mg, to describe the energy range from the VB to 320 eV the optimal radius was found to be $R = 2$ a.u., which for the bulk crystal results in 833 APWs for the hcp unit cell ($RG_{\rm max} = 11$) and requires the extension of the radial basis set [25] for orbitals up to $l = 10$. Finally, the basis set comprised 1577 functions per two atoms.

The huge basis set makes the embedding method [22] rather time consuming at high energies, so here it is used only below 160 eV (a fragment of an eight-layer slab is embedded). At higher energies, the simplified procedure that assumes a steplike potential barrier between bulk and vacuum is employed [21].

In the *ab initio* calculation, both for the initial and for the final states of photoemission a self-consistent crystal potential in the local density approximation (LDA) is used. The initial states are eigenfunctions of a finite slab: 197-a.u.-thick supercell (32-layer slab) for the true crystal and 246-a.u.-thick supercell for the 1DCP model. The respective potential profiles are shown in Fig. 1. Both slabs are thick enough to provide a reasonable approximation for the surface states, but to accurately determine the decay length one must use the true semi-infinite geometry. This is achieved with the embedding technique [22] (for the application to surface states, see Ref. [26]). The imaginary part of the wave vector for the true crystal was found to be $\kappa = 0.0086$ a.u.$^{-1}$, density decay length $(2\kappa)^{-1} = 58$ a.u. For 1DCP it was $\kappa = 0.0178$ a.u.$^{-1}$ and $(2\kappa)^{-1} = 27$ a.u., see the blue curves in Fig. 1.

The present all-electron calculation is in good agreement with the *ab initio* pseudopotential calculation of Ref. [27]. In particular, for the surface states, the density distribution parallel to the surface is virtually isotropic. Also the VB wave functions have quasi-1D character: in the Laue representation $\psi(\mathbf{r}) = \sum_{\mathbf{G}_\parallel} \psi_{\mathbf{G}_\parallel}(z) \exp(i\mathbf{G}_\parallel \mathbf{r}_\parallel)$ in terms of the surface reciprocal lattice vectors $\mathbf{G}_\parallel$ the $\mathbf{G}_\parallel = 0$ component constitutes, at least, 90%. However, as we will see in Sec. V, this does not mean that the $\mathbf{G}_\parallel \neq 0$ components can be neglected in photoemission: Indeed, in the Fourier decomposition of the function $\psi'_z(\mathbf{r})$ the weight of the $\mathbf{G}_\parallel \neq 0$ contribution ranges from 35% at the Fermi level to 90% at the VB bottom.

III. FOURIER ANALYSIS OF EIGENSTATES

Our aim is to understand what features of the true scattering state that distinguish it from a free electron are most relevant to the stationary photoemission, and how fast they disappear at high energies.

In the crystal half-space the final state reads

$$\Phi^*_{\mathrm{LEED}}(\mathbf{r}) = \sum_{k\in\mathrm{CBS}} \sum_{\mathbf{G}_\parallel g} \Phi^k_{\mathbf{G}_\parallel g} \exp[i(k+g)z + i\mathbf{G}_\parallel \mathbf{r}_\parallel]. \qquad (2)$$

Here $g = 2\pi n/c$ are the surface normal wave numbers. The scattering wave function is a superposition of a discrete set of the CBS partial waves $\phi(k, \mathbf{r})$, which are solutions of the Schrödinger equation with a complex potential $V_{\mathrm{B}}(\mathbf{r}) - iV_{\mathrm{i}}$ for a given (real) energy, where V_{B} is the three-dimensional (3D)-periodic potential of the bulk crystal and $-iV_{\mathrm{i}}$ is the spatially constant absorbing potential. In Fig. 2(a) CBS is shown as the dispersion $\mathrm{Re}\, k(E)$ for $V_{\mathrm{i}} = 0.5$ eV. The partial flux carried by a given wave [28,29] is indicated by the symbol size. The strongest contributing waves are seen to be located along the line $E(k) = (\hbar k)^2/2m + V_0$, with m being the true electron mass and the inner potential $V_0 = -9$ eV [red circles in Fig. 2(a)]. (All energies are relative to the Fermi level, unless stated otherwise.) The deviation of the actual Bloch vector k from the SFE value $k_{\mathrm{SFE}} = \sqrt{2m(E - V_0)}$ is shown in Fig. 2(b) for $V_{\mathrm{i}} = 0.5$, 2, and 5 eV: For a weakly absorbing potential the variations are on the order of ± 0.1 a.u.$^{-1}$. They become smoother with increasing V_{i}, and the deviation from the parabola stabilizes, but does not vanish, keeping the signature of the elastic multiple scattering. For example, around 300 eV the group velocity dE/dk_{SFE} derived from the parabolic fit is some 10% larger than the local dE/dk (in accord with the observation of Ref. [30] for WSe$_2$ where below 90 eV the free-electron fit was found to systematically overestimate the group velocity by 30%).

Alternatively to the complex-wave-vectors representation (2), each $\mathbf{G}_\parallel$ term of Φ^*_{LEED} can be written as a Fourier integral $\int F_{\mathbf{G}_\parallel}(q) \exp(iqz) dq$, where q is the wave number in the surface normal direction. This provides a descriptive picture of dipole transitions since $-i\hbar d/dz$ is diagonal in the q basis. In Mg(0001), over the whole energy interval the q spectrum is dominated by a single peak, see Fig. 2(c), with a nearly free-electron dispersion shown in Fig. 2(b). The importance of the resonant transitions (alias direct or vertical) depends on the strength of the higher g harmonics of the final and the initial state.

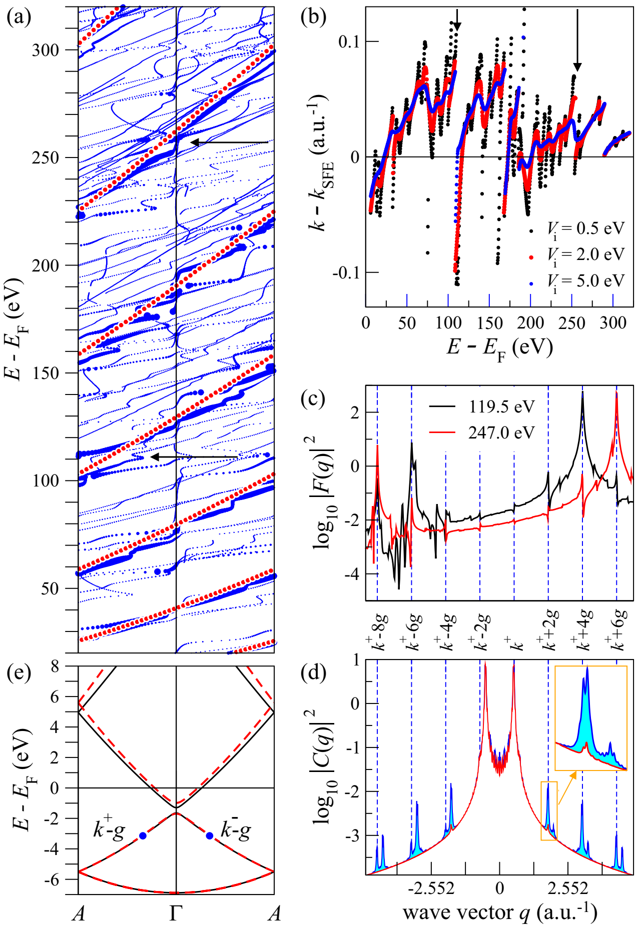

FIG. 2. (a) Conducting CBS $\mathrm{Re}\, k(E)$ of Mg(0001): The size of a blue circle is proportional to the partial flux carried by the respective Bloch wave. The red dotted line is a parabolic fit to the dispersion of the leading Bloch wave. (b) Deviation of the true dispersion of the leading Bloch wave from the parabolic fit. In graphs (a) and (b) arrows indicate the final states responsible for the spectral structures in Fig. 5(b). (c) Fourier spectra of the $G_\parallel = 0$ component of Φ^*_{LEED} for $E = 119.5$ eV (black) and 247.0 eV (red). (d) Fourier spectrum of the $G_\parallel = 0$ component of the slab eigenfunction at $E = -3.14$ eV: real crystal (blue) and 1DCP (red). The difference is highlighted by shading. The inset shows a magnified spectrum around $k^+ + 2g$. (e) Occupied bulk band structure of Mg along $A\Gamma A$: *ab initio* calculation (black lines) and 1DCP model (red dashed lines).

In a simple metal, the initial-state wave function sufficiently far from the surface is a superposition of a Bloch-wave k^+ incident onto the surface and k^- reflected into the interior of the crystal, see Fig. 2(e). Apart from that, at the surface, there is a contribution from an infinite number of the evanescent waves, which become important for a sufficiently small mean free path. Here, the initial states are represented by slab eigenfunctions. Figure 2(d) compares a Fourier spectrum of the state at $\mathbf{k}_\parallel = 0$ and $E = -3.14$ eV by the *ab initio* all-electron potential and by the 1DCP [23]. (To avoid the ambiguity of representing the discrete spectrum on a dense set of the supercell g numbers, the spectra are convoluted with a

Lorentzian of 0.02 a.u.$^{-1}$ FWHM). Because we are interested in dipole transitions, shown are the spectra of the function ψ'_z. Although the dispersion of the lower VB along $A\Gamma A$ in the 1DCP and in the *ab initio* calculations are identical, see Fig. 2(e), the higher harmonics of the pseudowave function are an order of magnitude weaker, so at high energies the direct transitions rapidly vanish. This was realized by the authors of Ref. [16], who added repulsive spikes to the 1DCP of Mg(0001) in order to enhance the higher harmonics.

IV. VOLUME AND SURFACE PHOTOEFFECT

Let us now apply the one-step theory of photoemission to the 1D and 3D crystals and compare the normal emission spectra in the extreme-ultraviolet range. The dependence of the intensity on the photon energy $\hbar\omega$ and initial energy E is shown in Fig. 3(a) for the 1DCP and in Fig. 3(b) for the real Mg(0001). For 1DCP the optical potential is $V_\mathrm{i} = 1$ eV (a typical value around 25 eV), and in the 3D calculation it is $V_\mathrm{i} = 3$ eV (an estimated average value in this energy interval). In 1DCP, the parabolic dispersion of the direct-transition peak persists up to $\hbar\omega \approx 50$ eV, above which the resonant transitions get exhausted, and the EDCs become structureless. The *ab initio* $I(E,\omega)$ is qualitatively different with rich structure and irregular dispersion—note the non-free-electron branch ξ and the intensity drop α (their origin will be discussed in detail in the next section, Fig. 5).

An important aspect, especially in the time-resolved spectroscopy, is how far from the surface the photoelectron originates. This depends on the photoelectron escape depth (eventually, on the inelastic-scattering rate expressed by the optical potential V_i) and on the shape of the exciting field. Let us exclude the latter factor and consider a homogeneous electric field normal to the surface, so the perturbation operator is $-i\hbar d/dz$. It may be recast as the potential gradient $(i/\omega)\hbar V'_z(\mathbf{r})$, which is a particularly transparent form for a semi-infinite jellium, where the only contribution to the matrix element comes from the surface barrier. Historically [32], this representation has been often drawn on to discriminate between the volume and the surface photoeffect [20,33]. (Not to be confused with the surface photoeffect due to the dielectric response [34], which is beyond the dipole approximation.) For a realistic crystal potential, the most natural way to assess the relative bulk and surface contributions to the photocurrent is to consider the dependence of the photocurrent on the absorbing potential V_i: A strong dependence on V_i implies a bulk origin, and a weak one is a signature of the surface photoeffect. This objective and transparent criterion was applied in Ref. [33] to a Kronig-Penney model. Let us compare from this point of view the real crystal and the 1DCP model.

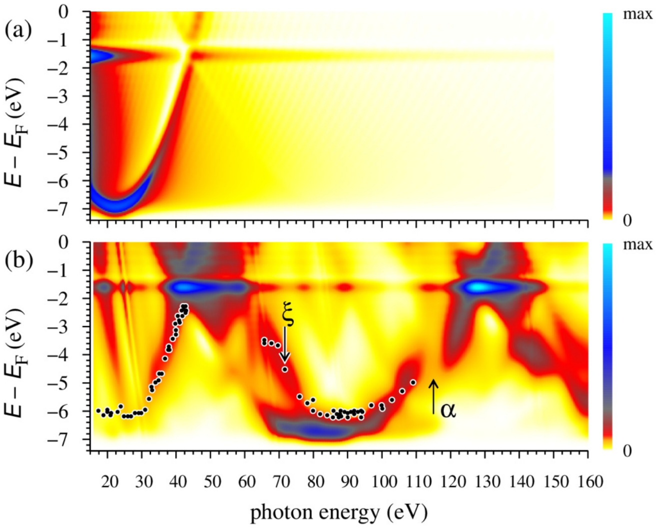

FIG. 3. Photocurrent distribution $I(E,\hbar\omega)$ in the 1DCP model (a) and in the full Φ^*_LEED calculation (b). Circles are experimental energy distribution curve (EDC) maxima [31]. (EDCs are cross-sections $\omega = \mathrm{const.}$)

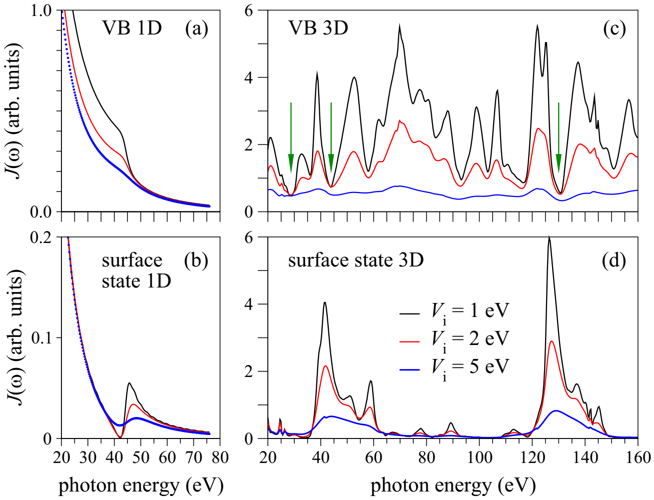

FIG. 4. Photoyield for three values of optical potential: $V_\mathrm{i} = 1$, 2, and 5 eV, given by black, red, and blue lines, respectively. (a) and (b): 1DCP [23]. (c) and (d): *ab initio* potential. (a) and (c): lower VB. (b) and (d): surface state. Arrows in graph (c) indicate the energies at which resonant transitions accidentally vanish.

Consider the photoyield $J(\omega)$ from the lower VB, i.e., the photocurrent summed over all the initial states. The $J(\omega)$ spectrum is especially instructive because its fine structure is not related to the direct-transition resonances: The k vectors of the initial states span the whole surface-perpendicular 1D Brillouin zone (BZ), so direct transitions occur at every ω. (The VB-integrated emission is relevant to attosecond spectroscopies, where the spectral width of the exciting pulse is comparable to the VB width.) Figures 4(a) and 4(c) show the VB $J(\omega)$ for the 1D and 3D cases, respectively. For the 1DCP, below $\hbar\omega = 45$ eV $J(\omega)$ decreases with V_i as is typical of direct transitions, and above 45 eV it becomes independent of V_i because the direct transitions are exhausted due to the deficiency of the higher g harmonics in the initial states [also reflected in the structure of the intensity map in Fig. 3(a)]. By contrast, in the 3D potential, the direct transitions dominate over the whole spectral range, and on average they do not weaken with increasing energy. In addition, the resonance character (quantified by the sensitivity to V_i) varies nonmonotonically with energy, and at certain energies the bulk contribution may accidentally vanish so that there only remain transitions to rapidly decaying evanescent states. Naturally

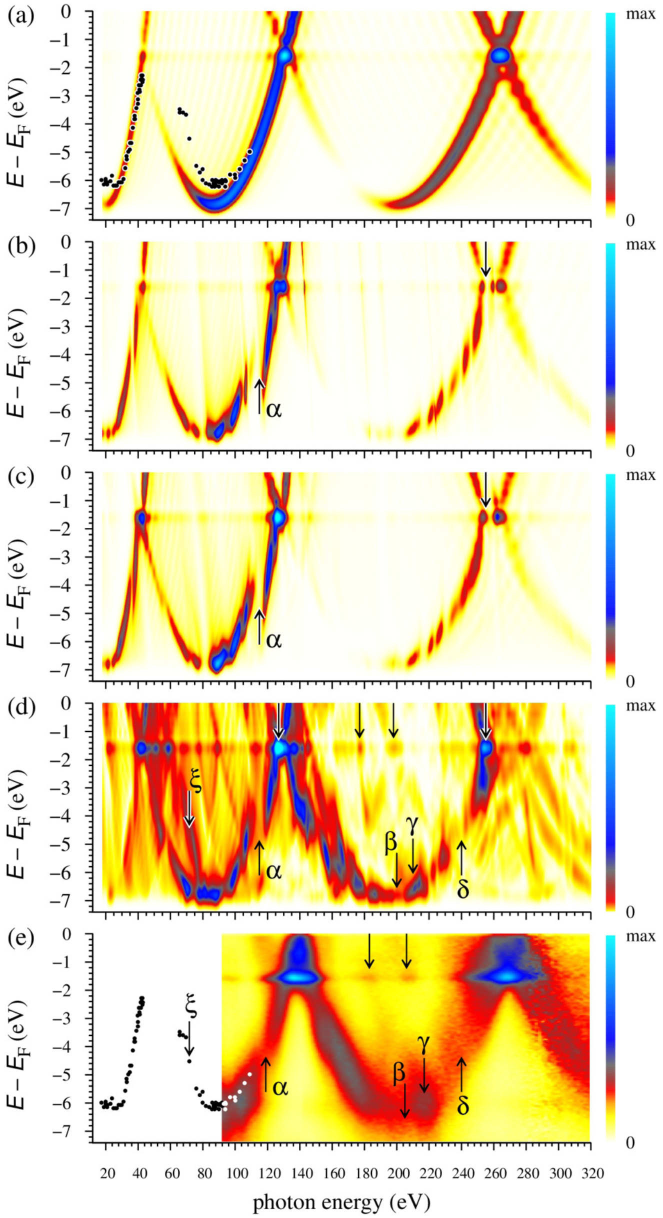

FIG. 5. Photocurrent distribution $I(E, \hbar\omega)$ in Mg(0001) for $V_i = 1$ eV. (a) Strictly free-electron final state. Circles are experimental EDC maxima [31]. (b) Single-plane-wave approximation with the actual dispersion $k(E)$. (c) Final state as a full $\mathbf{G}_\parallel = 0$ projected $\Phi^*_{\text{LEED}}(\mathbf{r})$. (d) Full $\Phi^*_{\text{LEED}}(\mathbf{r})$. (e) Experimental spectrogram [19]. Circles are the same as in graph (a). Arrows indicate the structures due to lattice scattering.

they correspond to intensity minima, indicated by arrows in Fig. 4(c).

Figures 4(b) and 4(d) illustrate the different behavior of the surface-state emission in the two models: In both systems there are no direct transitions below the resonance energy (46 eV for the 1DCP and 42 eV for the real crystal), but in the 1DCP the nonresonant excitations are much stronger than the resonant peak, whereas in the realistic model it is the other way around. Furthermore, the width of the resonance has different origin in the two models. In the 1DCP it is determined by the momentum broadening κ in the initial state. In the real crystal, κ is two times smaller, but the emission resonance is much wider, and it has a pronouncedly non-Lorentzian shape. This is because its width is determined by the structure of the final states (see also the discussion of the surface-state emission from Al(100) in Ref. [26]).

Thus, the 1DCP considerably overestimates the role of the nonresonant transitions in comparison to the realistic potential. To a certain extent this can be improved by using a harder 1D pseudopotential [16], however, the irregular oscillations of the yield and of the surface sensitivity are related to the 3D character of the final state as we will see in the next section.

V. APPROXIMATIONS TO THE FINAL STATE

In order to trace the fine structure of the intensity map in Fig. 3(b) to the composition of the initial and final states and to understand how detailed our knowledge of $\Phi^*_{\text{LEED}}(\mathbf{r})$ needs to be, let us consider the following steps of successive refinement of the final state: (i) a strictly free-electron solution $\exp(ik_{\text{SFE}}z)$ of the Hamiltonian $p^2/2m + V_0$, (ii) a single plane wave $\exp(ikz)$ with the actual dispersion $k(E)$, (iii) a full $\mathbf{G}_\parallel = 0$ component of $\Phi^*_{\text{LEED}}(\mathbf{r})$, and finally (iv) the full 3D $\Phi^*_{\text{LEED}}(\mathbf{r})$. To see if there is a trend towards simplification of the scattering functions with energy, we will now consider a wide region up to 320 eV, see Fig. 5.

The $\exp(ik_{\text{SFE}}z)$ approximation is shown in Fig. 5(a). It is physically similar to the 1DCP spectrogram in Fig. 3(a) in that it gives a plain Fourier image of the $\mathbf{G}_\parallel = 0$ component of the initial states [11]—SFE is characterized by the absence of a fine structure. In contrast to the 1DCP model, in real Mg(0001) the resonant transitions to SFE states persist up to high energies, reflecting the Fourier structure of the initial states. Note that while the lowermost ascending branch perfectly agrees with the experiment [35], the next parabola is considerably wider than the measured one, the descending branch of the latter being much steeper than the ascending branch.

For the SFE final states, the imaginary part of the wave-vector $k = k' + ik''$ varies smoothly with energy: $k'' \approx mV_i/(\hbar^2 k')$. This is not the case for the Bloch vector(s) of the true final state, which carr(y)ies the imprints of the band gaps and irregularities, see Fig. 2(b). Combining the single-plane-wave approximation with *ab initio* wave-numbers $k(E)$ already results in a rich fine structure in the spectrogram, see Fig. 5(b). Most significant features are the opening of a gap at $\hbar\omega = 115$ eV (denoted α) and the splitting of the surface state peak at 264 eV. [The relevant final states are indicated with arrows in Figs. 2(a) and 2(b).] Interestingly, using the full 1D function instead of the leading wave only slightly affects the spectrogram, see Fig. 5(c). Ultimately, the true 3D Φ^*_{LEED} dramatically changes the spectrogram: High intensity appears over the interval 140 to 190 eV, and a wide void δ occurs around 240 eV, both features being in accord with the experiment, Fig. 5(e). Note that from 140 to 190 eV the photocurrent is due exclusively to the $\mathbf{G}_\parallel \neq 0$ harmonics, so any 1D model will fail.

In addition, the lateral scattering gives rise to the steeply dispersing structure ξ and to the intensity oscillations β and γ. Also the $\hbar\omega$ dependence of the surface-state emission depends on the 3D structure of Φ^*_{LEED}: The third surface-state

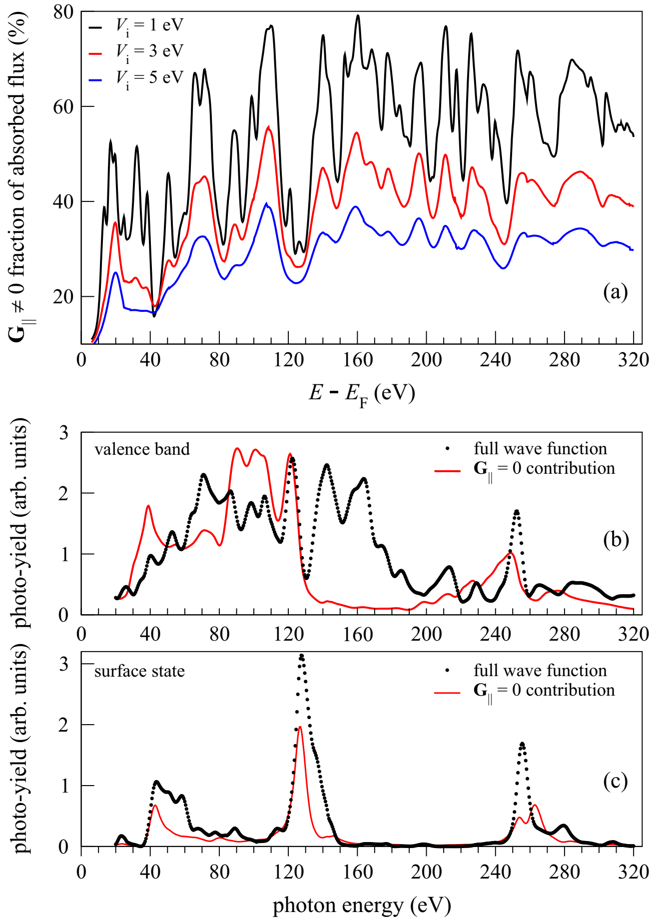

FIG. 6. Lateral Fourier analysis of the final-state wave function. (a) Energy dependence of the $\mathbf{G}_{\|} \neq 0$ fraction of the absorbed flux for $V_{\rm i} = 1$, 3, and 5 eV. (b) Photon-energy dependence of the normal-emission photoyield from the lower VB, see Fig. 2(e). (c) Photoyield from the surface state. In graphs (b) and (c) the dotted curves show the full photoyield, and the red lines show the $\mathbf{G}_{\|} = 0$ contribution.

TABLE I. Energies $\hbar\omega$ (eV) of the surface-state emission resonances in the experiments of Refs. [31]^a and [19]^b compared with the SFE model and with the *ab initio* calculations for $V_{\rm i} = 1$ and 3 eV. The $V_{\rm i} = 1$ eV values correspond to Figs. 5(a) (SFE) and 5(d) [full $\Phi^*_{\rm LEED}(\mathbf{r})$]. The values in the parentheses are the (more accurate) embedding calculation, see Figs. 3(b). In the full-$\Phi^*_{\rm LEED}(\mathbf{r})$ calculations the resonances are strongly asymmetric and several eV wide, see Fig. 4(d). Because reported are maxima rather than centers of gravity the variations of about 1 eV depending on $V_{\rm i}$ are insignificant. However, the differences of about 10 eV are significant.

Experiment	43.0^a	134.0^b	262.0^b
$V_{\rm i} = 1$ eV full $\Phi^*_{\rm LEED}$	41.8 (41.6)	126.5 (126.5)	254.5
$V_{\rm i} = 3$ eV full $\Phi^*_{\rm LEED}$	43.6 (42.2)	127.7 (128.0)	255.5
$V_{\rm i} = 1$ eV SFE	43.1	130.8	264.0
$V_{\rm i} = 3$ eV SFE	43.9	130.8	264.0

resonance moves from $\hbar\omega = 264$ eV (free-electron prediction) to 255 eV and two weaker maxima appear at 177 and 199 eV.

The dramatic difference between the 1D approximation [Fig. 5(c)] and the full 3D calculation [Fig. 5(d)] raises the question of whether the lateral scattering weakens with increasing the energy. Figure 6(a) shows the $\mathbf{G}_{\|} \neq 0$ fraction of the transmitted (absorbed) flux, which is expressed by the integral over the crystal half-space $T = (2V_{\rm i}/\hbar) \int |\Phi^*_{\rm LEED}(\mathbf{r})|^2 d\mathbf{r}$ [28,29]. At high energies, the $\mathbf{G}_{\|} \neq 0$ fraction shows neither an increasing nor a decreasing trend and oscillates around a constant level, which is the lower the larger the inelastic-scattering rate $V_{\rm i}$. The latter is known to grow increasingly slower at high energies [30], so the 3D character of the final state is expected to remain important over hundreds of eV. The implications for the photoemission intensities are illustrated in Figs. 6(b) and 6(c) by the photon energy dependence of the photo-yield $J(\omega)$, i.e., the photocurrent integrated over an initial-state band. For example, between 140 and 190 eV the $\mathbf{G}_{\|} = 0$ contribution to the matrix elements almost vanishes [cf. Figs. 5(c) and 5(d)], so the in-plane scattering is responsible for the entire intensity. It is equally important for the emission from the surface state [Fig. 6(c)]: although on a coarse scale the quasi-1D approximation gives the location of the $J(\omega)$ resonances with an accuracy of several eV, it does not correctly describe the width and the shape of the peaks.

In concluding this section, it should be mentioned that the pronounced spectral features caused by the lattice scattering are well documented experimentally: The non-free-electron branch ξ around $\hbar\omega = 70$ eV was experimentally observed in Ref. [31], and the intensity dips around $\hbar\omega = 115$, 200, and 240 eV (α, β, and δ) are well seen in the experimental spectrogram in Fig. 1(b) of Ref. [19]. Also the two weaker surface-state resonances at 177 and 199 eV have their distinct counterparts in the measurements of Ref. [19], at 183 and 206 eV, see Fig. 5(e). The precise knowledge of the energy location and the shape of the surface resonances and pronounced intensity dips is indispensable in order to correctly extract the real part of the quasiparticle self-energy in this region, which is still little known about theoretically. These features prove to be sensitive to the details of the final-state wave function, see Table I; in particular, the free-electron approximation is seen to be especially inaccurate *at the higher energies*, where it makes an error of 10 eV in the location of the surface-state resonance. Note that the SFE values are closer to the experiment, which may produce a misleading impression that the free-electron model agrees with the experiment. In fact, the discrepancy between the experiment and the *ab initio* calculation is due to the deficiency of the LDA potential being used instead of an accurate self-energy (empirically, the error grows approximately as $0.04(E - E_{\rm F})$ [36,37]). In this regard, it should be mentioned that the perfect agreement between theory and experiment in the dispersion of the lowermost parabola [Figs. 3(b) and 5(a)] is somewhat deceiving: In the LDA, the VB of Mg is some 0.6 eV wider than in the experiment, and upon correcting for this discrepancy one would reveal a self-energy shift of the LDA final states.

To summarize, the free-electron final state can be relied upon in giving a rough picture of the dispersion of the intensity distribution over a range of hundreds of eV, but this approximation is not sufficient on a finer scale of several eV.

VI. FINAL STATES AND WIGNER DELAY

In the previous sections we discussed the stationary photocurrent, which is given by the square modulus of the matrix element. In that case the spatial aspect of the excitations is limited to the effect of a finite mean free path on the EDCs. Complementary information about the spatial localization of the excitation is contained in phase η of the matrix element, whose energy derivative is relevant to the photoelectron escape time τ, i.e., the time it takes the photoelectron to move away from the surface to a certain distance into vacuum after the excitation. The escape time can, in principle, be inferred from a streaking experiment [14,18,19,36,38,39]. For a sufficiently spectrally narrow perturbation, τ can be calculated by the Wigner delay formula $\tau = d\eta/dE$ [36]. If the reference plane (at which τ is measured) is chosen to coincide with the onset of the optical potential, see Fig. 1, for the bulk-continuum states the average escape depth is just the photoelectron mean free path λ. In a semiclassical picture, λ is a product of the group velocity and the electron lifetime $\hbar/2V_\mathrm{i}$, so the escape time simply equals the lifetime [39]. Figure 7 shows the calculated escape time τ averaged over the lower VB and separately for the surface state (τ is given in attoseconds, 1 as $= 10^{-18}$ s). The calculations are for the 1DCP and for the 3D potential (including the true surface barrier [22]). In the 1D model, both for the VB and for the surface state, the onset of the purely indirect transitions is clearly seen at 50 eV, see Figs. 7(a) and 7(b): The nonresonant excitations are characterized by a very short and energy-independent τ, indicating their surface origin. By contrast, for the resonant transitions at the lower energies, τ decreases with V_i similar to the 3D result and roughly in accord with the semiclassical expectations [the $\hbar/2V_\mathrm{i}$ values are shown in Figs. 7(a) and 7(c)]. For the 3D potential, τ everywhere decreases with V_i as expected in view of the dominant role of the bulk transitions over the whole range, in accord with the previous section. Regarding the surface-state emission, both calculations agree in that it has the *bulk* origin, which is not surprising since the decay length of the surface state (27 a.u. in the 1D model and 58 a.u. in the real crystal) is larger than the mean free path at $E = 40$ eV: For $V_\mathrm{i} = 2$ eV it is $\lambda = 12$ a.u.

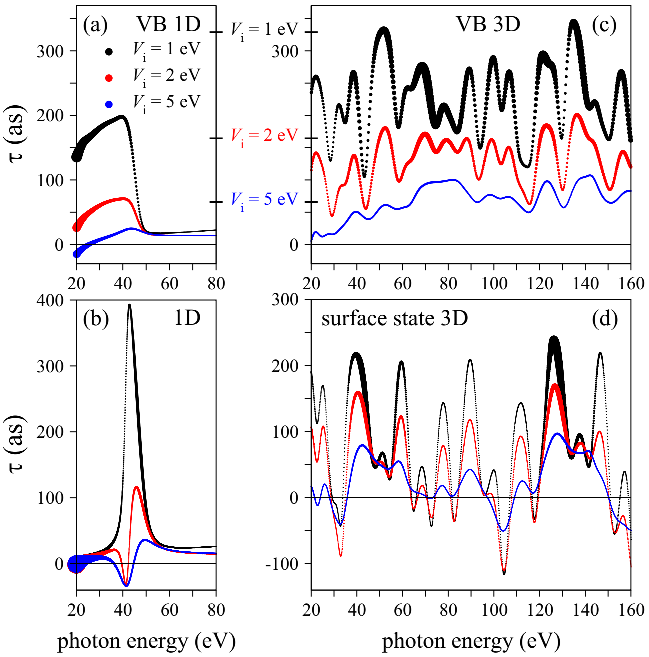

FIG. 7. Wigner delay τ as a function of the photon energy for the (a) and (b) 1DCP model, and for the (c) and (d) 3D potential. Graphs (a) and (c) show τ averaged over the lower VB, and graphs (b) and (d) show τ for the surface state. The curves are for three values of V_i: 1 (black), 2 (red), and 5 eV (blue). The respective $\hbar/2V_\mathrm{i}$ values are shown by the thicker ticks in graphs (a) and (c). The size of the symbols is proportional to the photoyield, see Fig. 4.

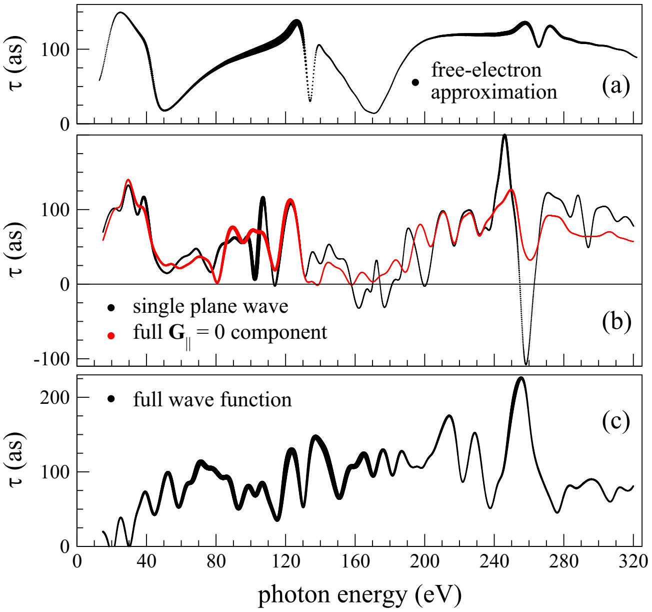

FIG. 8. Photon-energy dependence of the Wigner delay for $V_\mathrm{i} = 3$ eV. (a) Strictly free-electron final state. (b) Single-plane-wave approximation with the actual dispersion $k(E)$ (black) and final state as a full $\mathbf{G}_\parallel = 0$ component of $\Phi^*_\mathrm{LEED}(\mathbf{r})$ (red). (c) Full $\Phi^*_\mathrm{LEED}(\mathbf{r})$. The size of the circles is proportional to the respective photoyield.

Let us now turn to the true 3D initial states and analyze the *ab initio* $\tau(E)$ curves from the point of view of the composition of the final states, considering the same approximations as in Fig. 5, see Sec. V. Figure 8(a) shows $\tau(E)$ for the strictly free-electron final states. It reveals the Fourier structure of the $\mathbf{G}_\parallel = 0$ component of the initial states, which is seen to cause long-range variations of τ of a magnitude of about 100 as (for $V_\mathrm{i} = 3$ eV). Also note that the sharp minimum at 134 eV occurs very close to the minimum in the respective curve in a modified 1D model of Mg(0001) [16], Fig. 3(b) in that work. There a harder 1D pseudopotential was used, which strengthens the higher-g harmonics in the initials states but apparently leaves the final states practically identical to plane waves.

The further refinement of the single-$\mathbf{G}_\parallel$ approximation, namely, by taking into account the correct dispersion $k(E)$ and then including the higher-g components, does not change the long-range behavior but introduces short-range variations on the scale of several eV, Fig. 8(b). However, the inclusion of the $\mathbf{G}_\parallel \neq 0$ components dramatically changes the picture over the whole range, Fig. 8(c): Even the long-range structure of the $\tau(\omega)$ curve bears no resemblance to that of the approximate curves. This means that 1D models are genuinely insufficient to describe the temporal aspects of photoemission even for a simple metal.

VII. DISCUSSION AND CONCLUSIONS

The above analysis clarifies the notion of a nearly free-electron motion in application to photoemission. A careful look at the composition of the outgoing wave reveals the essential distinction between the strictly free-electron and realistic free-electron-like wave function. The two behave similarly on a rough energy scale of hundreds of eV, so the experimental dispersion of the EDC peaks measured over an interval of 500 eV gives a realistic estimate of the surface-perpendicular BZ. However, this should not create the illusion that a single-plane-wave approximation may be reliable locally, on a scale of several eV. Indeed, the lattice scattering leads to strong irregular oscillations of the photoemission intensity (Fig. 5), the spectral structures being of two kinds: Some features are caused by sharp deviations of the leading wave from a parabolic dispersion [Fig. 2(b)], whereas the origin of the other ones is hidden in the structure of the wave functions. In the present calculation one structure of the first kind is unambiguously identified: The intensity dip at $\hbar\omega = 115$ eV [Fig. 3(b)], which is confirmed by the experiment [19]. Such structures are ubiquitous at lower energies, and they are known to manifest themselves in electron transmission spectra [40]. However, it follows from simple perturbational reasoning that at sufficiently high energies the deviations from the parabolic dispersion become less and less important, furthermore, at high energies they are more easily blurred by correlated lattice vibrations [41].

More important turns out to be the effect of the in-plane scattering, i.e., the $\mathbf{G}_\parallel \neq 0$ contribution to the wave function. It is responsible for the rich fine structure of the spectrogram up to the highest energy studied [Fig. 5(d)], and there is no reason to expect that this factor would become less significant at the higher energies. The in-plane scattering is found to especially strongly influence the photoelectron dynamics. The key quantity here is the Wigner delay, for which the neglect of the $\mathbf{G}_\parallel \neq 0$ components leads to a qualitatively different dependence $\tau(\omega)$ even on a coarse scale (Fig. 8). This sheds some doubt on the general applicability of 1D models to a material-specific simulation of the photoelectron transport, in particular, in the context of the laser streaking spectroscopy. Apart from giving rather unreliable $\tau(\omega)$ values, the 1D models that employ a shallow potential strongly overestimate the role of the surface photoeffect in comparison to the real crystals whereby the photoelectron transport in the 1D models proceeds very differently from that in a 3D singular potential.

The present paper is limited to the lower part of the soft x-ray spectrum because of the brute-force Bloch-waves method used to compute the LEED states. An advantage of this procedure is that it yields the results with the accuracy of the underlying high-energy band structure (which can be verified by alternative band-structure methods) and provides a benchmark for various approximations to the outgoing wave, such as the single-scatterer approach [42] often used in multiple-scattering theories. Furthermore, it gives a clear indication of the importance of the intralayer scattering also at much higher energies, especially for heavier atoms. Being unaware of the importance of the wave function details would make it puzzling to interpret soft x-ray spectra as the main structures expected from resonant transitions may appear missing or shifted by several eV.

ACKNOWLEDGMENTS

The author is grateful to R. Kuzian, I. Nechaev, V. Silkin, and V. Strocov for comments and suggestions during the preparation of this paper. The author thanks P. Feulner, S. Neppl, and J. Riemensberger for explaining the details of their experiment [19] and providing the original data and V. Silkin for providing the numerical data of the 1DCP pseudopotential. This work was supported by the Spanish Ministry of Science and Innovation (Project No. PID2019-105488GB-I00).

---

[1] V. N. Strocov, T. Schmitt, U. Flechsig, T. Schmidt, A. Imhof, Q. Chen, J. Raabe, R. Betemps, D. Zimoch, J. Krempasky, X. Wang, M. Grioni, A. Piazzalunga, and L. Patthey, High-resolution soft X-ray beamline ADRESS at the Swiss Light Source for resonant inelastic X-ray scattering and angle-resolved photoelectron spectroscopies, J. Synchrotron Radiat. **17**, 631 (2010).

[2] C. Fadley, X-ray photoelectron spectroscopy: Progress and perspectives, J. Electron Spectrosc. Relat. Phenom. **178–179**, 2 (2010).

[3] S. Suga and A. Sekiyama, *Photoelectron Spectroscopy Bulk and Surface Electronic Structures*, Springer Series in Optical Sciences, Vol. 176 (Springer-Verlag, Berlin/Heidelberg, 2014).

[4] S. Suga and C. Tusche, Photoelectron spectroscopy in a wide $h\nu$ region from 6 eV to 8 keV with full momentum and spin resolution, J. Electron Spectrosc. Relat. Phenom. **200**, 119 (2015), special Anniversary Issue: Volume 200.

[5] S. Hüfner, *Photoelectron Spectroscopy Principles and Applications*, Advanced Texts in Physics (Springer-Verlag, Berlin/Heidelberg, 2003).

[6] P. Hofmann, C. Søndergaard, S. Agergaard, S. V. Hoffmann, J. E. Gayone, G. Zampieri, S. Lizzit, and A. Baraldi, Unexpected surface sensitivity at high energies in angle-resolved photoemission, Phys. Rev. B **66**, 245422 (2002).

[7] F. Venturini, J. Minár, J. Braun, H. Ebert, and N. B. Brookes, Soft x-ray angle-resolved photoemission spectroscopy on Ag(001): Band mapping, photon momentum effects, and circular dichroism, Phys. Rev. B **77**, 045126 (2008).

[8] V. N. Strocov, M. Shi, M. Kobayashi, C. Monney, X. Wang, J. Krempasky, T. Schmitt, L. Patthey, H. Berger, and P. Blaha, Three-Dimensional Electron Realm in VSe$_2$ by Soft-X-Ray Photoelectron Spectroscopy: Origin of Charge-Density Waves, Phys. Rev. Lett. **109**, 086401 (2012).

[9] O. Fedchenko, K. Medjanik, S. Chernov, D. Kutnyakhov, M. Ellguth, A. Oelsner, B. Schönhense, T. R. F. Peixoto, P. Lutz, C.-H. Min, F. Reinert, S. Däster, Y. Acremann, J. Viefhaus, W. Wurth, J. Braun, J. Minár, H. Ebert, H. J. Elmers, and G. Schönhense, 4D texture of circular dichroism in soft-x-ray photoemission from tungsten, New J. Phys. **21**, 013017 (2019).

[10] R. P. Day, B. Zwartsenberg, I. S. Elfimov, and A. Damascelli, Computational framework chinook for angle-resolved photoemission spectroscopy, npj Quantum Mater. **4**, 54 (2019).

[11] V. Strocov, Photoemission response of 2D electron states, J. Electron Spectrosc. Relat. Phenom. **229**, 100 (2018).

[12] J. Braun, J. Minár, and H. Ebert, Correlation, temperature and disorder: Recent developments in the one-step description of angle-resolved photoemission, Phys. Rep. **740**, 1 (2018).

[13] J. Braun, J. Minár, and H. Ebert, One Step Model Description of HARPES: Inclusion of Disorder and Temperature Effects, in *Hard X-ray Photoelectron Spectroscopy*, edited by J. C. Woicik, Springer Series in Surface Sciences, Vol. 59 (Springer-Verlag, Berlin/Heidelberg, 2016), pp. 159–174.

[14] R. Pazourek, S. Nagele, and J. Burgdörfer, Attosecond chronoscopy of photoemission, Rev. Mod. Phys. **87**, 765 (2015).

[15] Q. Liao, W. Cao, Q. Zhang, K. Liu, F. Wang, P. Lu, and U. Thumm, Distinction of Electron Dispersion in Time-Resolved Photoemission Spectroscopy, Phys. Rev. Lett. **125**, 043201 (2020).

[16] A. G. Borisov, D. Sánchez-Portal, A. K. Kazansky, and P. M. Echenique, Resonant and nonresonant processes in attosecond streaking from metals, Phys. Rev. B **87**, 121110(R) (2013).

[17] Q. Liao and U. Thumm, Initial-state, mean-free-path, and skin-depth dependence of attosecond time-resolved ir-streaked xuv photoemission from single-crystalline magnesium, Phys. Rev. A **89**, 033849 (2014).

[18] S. Neppl, R. Ernstorfer, E. M. Bothschafter, A. L. Cavalieri, D. Menzel, J. V. Barth, F. Krausz, R. Kienberger, and P. Feulner, Attosecond Time-Resolved Photoemission from Core and Valence States of Magnesium, Phys. Rev. Lett. **109**, 087401 (2012).

[19] J. Riemensberger, S. Neppl, D. Potamianos, M. Schäffer, M. Schnitzenbaumer, M. Ossiander, C. Schröder, A. Guggenmos, U. Kleineberg, D. Menzel, F. Allegretti, J. V. Barth, R. Kienberger, P. Feulner, A. G. Borisov, P. M. Echenique, and A. K. Kazansky, Attosecond Dynamics of *sp*-Band Photoexcitation, Phys. Rev. Lett. **123**, 176801 (2019).

[20] I. Adawi, Theory of the surface photoelectric effect for one and two photons, Phys. Rev. **134**, A788 (1964).

[21] E. E. Krasovskii and W. Schattke, Calculation of the wave functions for semi-infinite crystals with linear methods of band theory, Phys. Rev. B **59**, R15609(R) (1999).

[22] E. E. Krasovskii, Augmented-plane-wave approach to scattering of Bloch electrons by an interface, Phys. Rev. B **70**, 245322 (2004).

[23] E. Chulkov, V. Silkin, and P. Echenique, Image potential states on metal surfaces: binding energies and wave functions, Surf. Sci. **437**, 330 (1999).

[24] E. E. Krasovskii and W. Schattke, Surface electronic structure with the linear methods of band theory, Phys. Rev. B **56**, 12874 (1997).

[25] E. E. Krasovskii, Accuracy and convergence properties of the extended linear augmented-plane-wave method, Phys. Rev. B **56**, 12866 (1997).

[26] E. E. Krasovskii and W. Schattke, Angle-Resolved Photoemission from Surface States, Phys. Rev. Lett. **93**, 027601 (2004).

[27] E. Chulkov and V. Silkin, AB initio calculation of the surface electronic structure of Mg(0001), Solid State Commun. **58**, 273 (1986).

[28] V. N. Strocov, H. I. Starnberg, and P. O. Nilsson, Excited-state bands of Cu determined by VLEED band fitting and their implications for photoemission, Phys. Rev. B **56**, 1717 (1997).

[29] V. N. Strocov, E. E. Krasovskii, W. Schattke, N. Barrett, H. Berger, D. Schrupp, and R. Claessen, Three-dimensional band structure of layered TiTe_2: Photoemission final-state effects, Phys. Rev. B **74**, 195125 (2006).

[30] V. Silkin, E. Krasovskii, E. Chulkov, and P. Echenique, Dynamics and mean-free path of electronic excitations in WSe_2, Surf. Sci. **678**, 72 (2018).

[31] R. A. Bartynski, R. H. Gaylord, T. Gustafsson, and E. W. Plummer, Angle-resolved photoemission study of the surface and bulk electronic structure of Mg(0001) and Mg(1120), Phys. Rev. B **33**, 3644 (1986).

[32] I. Tamm and S. Schubin, Zur Theorie des Photoeffektes an Metallen, Z. Phys. **68**, 97 (1931).

[33] W. L. Schaich and N. W. Ashcroft, Model calculations in the theory of photoemission, Phys. Rev. B **3**, 2452 (1971).

[34] P. J. Feibelman, Self-Consistent Calculation of the Surface Photoelectric Effect, Phys. Rev. Lett. **34**, 1092 (1975).

[35] The data are reproduced from Fig. 6 in Ref. [31] with uncertainty within ±0.05 eV.

[36] R. O. Kuzian and E. E. Krasovskii, One-step theory of photoelectron escape time: Attosecond spectroscopy of Mg(0001), Phys. Rev. B **102**, 115116 (2020).

[37] E. E. Krasovskii, W. Schattke, P. Jiříček, M. Vondráček, O. V. Krasovska, V. N. Antonov, A. P. Shpak, and I. Bartoš, Photoemission from Al(100) and (111): Experiment and ab initio theory, Phys. Rev. B **78**, 165406 (2008).

[38] F. Siek, S. Neb, P. Bartz, M. Hensen, C. Strüber, S. Fiechter, M. Torrent-Sucarrat, V. Silkin, E. Krasovskii, N. Kabachnik, S. Fritzsche, R. Muiño, P. Echenique, A. Kazansky, N. Müller, W. Pfeiffer, and U. Heinzmann, Angular momentum-induced delays in solid-state photoemission enhanced by intra-atomic interactions, Science **357**, 1274 (2017).

[39] E. E. Krasovskii, C. Friedrich, W. Schattke, and P. M. Echenique, Rapid propagation of a Bloch wave packet excited by a femtosecond ultraviolet pulse, Phys. Rev. B **94**, 195434 (2016).

[40] V. N. Strocov, H. I. Starnberg, P. O. Nilsson, H. E. Brauer, and L. J. Holleboom, New Method for Absolute Band Structure Determination by Combining Photoemission with Very-Low-Energy Electron Diffraction: Application to Layered VSe_2, Phys. Rev. Lett. **79**, 467 (1997).

[41] L. Plucinski, J. Minár, B. C. Sell, J. Braun, H. Ebert, C. M. Schneider, and C. S. Fadley, Band mapping in higher-energy x-ray photoemission: Phonon effects and comparison to one-step theory, Phys. Rev. B **78**, 035108 (2008).

[42] S. Kono, S. M. Goldberg, N. F. T. Hall, and C. S. Fadley, Chemisorption geometry of $c(2 \times 2)$ oxygen on Cu (001) from angle-resolved core-level x-ray photoemission, Phys. Rev. B **22**, 6085 (1980).